Article

Ga-doped and Pt-loaded Porous TiO2-SiO2 for Photocatalytic Nonoxidative Coupling of Methane

wu shiqun, Xianjun Tan, Juying Lei, Haijun Chen, Lingzhi Wang, and Jinlong Zhang

J. Am. Chem. Soc., **Just Accepted Manuscript** • Publication Date (Web): 29 Mar 2019

Ga-doped and Pt-loaded Porous TiO_2-SiO_2 for Photocatalytic Nonoxidative Coupling of Methane

Shiqun Wu[a], Xianjun Tan[c], Juying Lei[a], Haijun Chen[b], Lingzhi Wang,[a]* Jinlong Zhang[a]*

[a] Key Laboratory for Advanced Materials and Institute of Fine Chemicals, School of Chemistry and Molecular Engineering, East China University of Science and Technology, 130 Meilong Road, Shanghai 200237 (P.R. China)

[b] Department of Electronics and Tianjin Key Laboratory of Photo-Electronic Thin Film Device and Technology, Nankai University, Tianjin, 300071 (P. R. China)

[c] Key Lab of Low-Carbon Conversion Science and Engineering, Shanghai Advanced Research Institute, Chinese Academy of Sciences, Shanghai 201210 (P. R. China)

***Keywords**: methane conversion• photocatalysis • gallium doping• oxygen vacancy • Pt loading*

ABSTRACT: Photodriven nonoxidative coupling of CH_4 (NOCM) is a potential alternative approach to clean hydrogen and hydrocarbon production. Herein, a Mott-Schottky photocatalyst for NOCM is fabricated by loading Pt nanoclusters on a Ga-doped hierarchical porous TiO_2-SiO_2 microarray (HGTS) with an anatase framework, which exhibits a CH_4 conversion rate of 3.48 $\mu molg^{-1}h^{-1}$ with 90% selectivity towards C_2H_6. This activity is 13 times higher than those from microarrays without Pt and Ga. Moreover, a continuous H_2 production (36 $\mu molg^{-1}$) with a high CH_4 conversion rate of approx. 28% can be achieved through a longtime irradiation (32 h). The influence of Ga on the chemical state of a surface oxygen vacancy (Vo) and deposited Pt is investigated through a combination of experimental analysis and first-principles density functional theory calculations. Ga substitutes for the five-coordinated Ti next to Vo, which tends to stabilize the single-electron trapped Vo and reduce the electrons transfer from Vo to the adsorbed Pt, resulting in the formation of a higher amount of cationic Pt. The cationic Pt and electron-enriched metallic Pt form a cationic-anionic active pair, which is more efficient for the dissociation of C-H bonds. However, the presence of too much cationic Pt results in more C_{2+} product with a decrease in the CH_4 conversion rate due to the reduced charge-carrier separation efficiency. This study provides deep insight into the effect of the doping/loading strategy on the photocatalytic NOCM reaction and is expected to shed substantial light on future structural design and modulation.

INTRODUCTION

Methane is a promising energy source with huge reserves and is considered as one of the alternatives to nonrenewable petroleum resources, since it can be converted to valuable hydrocarbon feedstocks and hydrogen through appropriate reactions.[1-6] Nonoxidative coupling of methane (NOCM) has proven to be a promising approach to methane conversion for C_2 products and hydrogen.[7-10] However, a high activation temperature is required to trigger this reaction owing to the tremendous thermodynamic barrier, which often causes coke deactivation of the catalyst and low selectivity.[11] Therefore, there is an urgent demand to develop new strategies for NOCM under mild conditions.

Photocatalysis is a green technology for C1 conversion, which can significantly lower the reaction temperature.[12-15] Until now, several photocatalysts have been developed for NOCM reactions including silica-alumina-titania,[16, 17] silica-supported oxides,[18, 19] and ceria-based[9, 20] and zeolite-based photocatalysts.[21] For examples, Yoshida et al. achieved an effective C_2H_6 production (0.69 $\mu molg^{-1}h^{-1}$) on the ternary oxide SiO_2-Al_2O_3-TiO_2 under Xe lamp irradiation.[16] Chen et al. achieved an extremely high CH_4 conversion rate of 29.8 $\mu molg^{-1}h^{-1}$ for NOCM under UV irradiation using Ga^{3+}-modified ETS-1 as the photocatalyst.[22] Very recently, Yi et al. reported an efficient CH_4 combustion on a Ag-ZnO composite, which is also active for NOCM with a comparatively low conversion rate of 0.35%.[23] The surface defects including Vo and Zn^+ play a vital role in the CH_4 photooxidation, and Ag endows a visible-light activity due to the surface plasmon effect. Meanwhile, Long et al. revealed the high efficiency of Au/ZnO for NOCM benefitting from the surface plasmon effect of Au, while the effect from defects is excluded through EPR analysis.[24] The above studies have demonstrated the feasibility of traditional doping/loading strategies on enhancing the photocatalytic NOCM efficiency. However, compared with those for other C1 conversions, the available active structures for photocatalytic CH_4 conversion are still in short supply. Moreover, the influence of doping/loading on the band structure, surface atomic arrangement and electronic characteristics of semiconductors and their relation with C-H activation and NOCM selectivity remain quite ambiguous, requiring a long-standing effort to explore.

Herein, a Ga-doped TiO_2-SiO_2 microarray with a hierarchical macro-mesoporous structure (HGTS) is developed for NOCM. Pt nanoclusters, as a commonly used cocatalyst for the photocatalytic hydrogen evolution reaction, are further deposited (Pt/HGTS) to explore their effect on NOCM. A high CH_4 conversion rate of 3.48 $\mu molg^{-1}h^{-1}$ for the

selective production of C_2H_6 is achieved at room temperature. Moreover, a steady H_2 yield of 36 μmolg^{-1} within 32 h is attained and is accompanied by a high CH_4 conversion percentage of 28% without loss of structural stability. The successive influence of Ga doping on the characteristics of surface Vo, Pt deposition and NOCM efficiency are explicitly unraveled by combining analyses of XPS, EPR and first-principles density functional theory (DFT) calculations.

EXPERIMENTAL SECTION

Chemicals. Sodium dodecyl sulfate (SDS, AR), styrene (AR), potassium persulfate (KPS, AR) and Pluronic triblock copolymer P123 ($EO_{20}PO_{70}EO_{20}$, Mav=5800) were purchased from Sigma-Aldrich. Titanium isopropoxide (TTIP, AR) was purchased from Adamas-beta. Gallium nitrate hydrate ($Ga(NO_3)_3$•xH_2O, AR) was purchased from Sinopharm chemical reagent Co., Ltd. Titanium tetrachloride ($TiCl_4$, AR), tetraethyl orthosilicate (TEOS, AR) and ethanol (EtOH, AR) were obtained from Aladdin. Ultrahigh purity CH_4 (99.99%) was purchased from Shanghai Shenkai Gases Technology Company. Chloroplatnic acid hexahydrate (H_2PtCl_6•$6H_2O$, Pt>37.5%) and ultrapure water were used without any further purification.

Preparation of PS: Generally, polystyrenes were employed as hard templates to generate macropores. First, 0.45 g of SDS and 0.6 g of KPS were dissolved in 118.5 g of EtOH and 270 g of H_2O in a 500-mL three-neck flask and stirred for 30 min. Then, the flask was evacuated and charged with N_2 to 1 bar. The flask was heated to 344 K, and 32.7 g of fresh washed styrene was injected. The reaction was finished after 19 h. The polystyrene opals were obtained by drying the polystyrene emulsion in a 343 K oven for 3 days.

Preparation of HTS, HGTS and MGTS: The hierarchical ordered TiO_2-SiO_2 composites (HTS) were synthesized by the evaporation-induced self-assembly (EISA) method. Typically, the Ti-Si precursor was synthesized by mixing together 2 g of P123, 23.7 g of EtOH, 0.83 g of TEOS, 0.92 g of $TiCl_4$ and 3.2 g of TTIP. The precursor was stirred at 298 K for 4 h, and then the polystyrene opals were immersed into the precursor, which was evaporated at 341 K and 55% relative humidity over 3 days and then dried at 340 K for 3 days. The obtained blocks were calcined at 773 K for 5 h with a heating rate of 1 K/min. After that, the samples were collected and washed with water 2 times for further use; the samples are denoted as HTS. For the preparation of HGTS, the process was the same except that different quantities of $Ga(NO_3)_3$•xH_2O were added to the Ti-Si precursor. For the preparation of MGTS, the process was the same except that there was no PS template.

Preparation of TS-1: Microporous titanosilicate (TS-1), with a BET surface of 423 m^2/g, was prepared by combining 11.3 g of TEOS and 0.61 g of TBOT and stirring for 1 h. H_2O (5 g) was dropped into 5 g of tetrapropylammonium hydroxide (40 wt%) and stirred for 1 h. The titanium silicate was slowly dropped into the tetrapropylammonium hydroxide solution, and within 1 h, 9.7 g of H_2O was dropped into it; the solution was stirred for 2 h, and then the temperature was increased to 333 K for 0.5 h. The temperature was increased to 348 K and kept for 3 h to remove the ethanol while 10 g of H_2O was slowly dropped into it. The above products were placed in a hydrothermal kettle and held at 573 K for 2 days. The product was obtained by centrifuging and washing with EtOH and H_2O 3 times and then dried in a vacuum overnight.

Preparation of Pt/HTS and Pt/HGTS: Pt/HTS and Pt/HGTS were prepared through a photodeposition method. Typically, 0.2 g of HTS or HGTS was dissolved in 20 g of H_2O and 15.8 g of EtOH. After that, 6.64 mL of a H_2PtCl_6•$6H_2O$ aqueous solution (1 g/L) (corresponding to a 1 wt% loading amount) was added to the mixture. The mixture was stirred for 30 min and then irradiated by a 300 W xenon lamp for 1 h. The product was obtained by centrifuging the crude product with EtOH and H_2O 3 times and was then dried in a vacuum overnight.

NOCM Reaction Test and Calculation of Conversion and Selectivity: A 0.2-g solid sample was added to a closed quartz reaction vessel (45 cm^3), which was then evacuated for 10 min to remove air. Afterwards, 44.6 μmol of pure methane (99.99%) was injected into the vessel by a gas injection needle and stirred for 1 h to achieve an adsorption-desorption balance. The vessel was irradiated by a 300-W Xe lamp for 4 h. Before the photocatalytic NOCM reaction, all the samples had been evacuated in a tube furnace at 393 K for 4 h to remove the adsorbed water and other molecules. The temperature of the reactor under photoirradiation was measured to be approximately 333 K. The hydrocarbon products were obtained by heating the reaction vessel at 523 K for 30 min for desorption and then analyzed by gas chromatography (GC) with a flame-ionization detector (FID). Hydrogen was analyzed by GC with a high-sensitivity thermal conductivity detector (TCD). The relative deviation of detection was less than 5% for GC.

Calculation of Conversion and Selectivity: The conversion of methane refers to the moles of methane consumed in reaction to the initial total moles of methane before reaction (Equation 1). The selectivity for ethane refers to the moles of obtained ethane to the total moles of all obtained hydrocarbon products in terms of carbon (Equation 2).

Equation 1:

$$\text{Conversion} = 100\% \times \text{Consumed methane}/\text{Added methane}$$

Equation 2:

$$\text{Selectivity} = 100\% \times \text{Obtained ethane}/\text{All hydrocarbon products}$$

Density functional theory calculations: Calculations for the total energy and electronic structure were carried out using the CASTEP program within the framework of density functional theory (DFT). [25, 26] The ultrasoft pseudopotential was used for electron-ion interactions, and the Perdew-Burke-Ernzerhof (PBE) form of the generalized gradient approximation (GGA) was employed to describe the exchange-correlation functional.[27] For the C-H dissociation and TS search calculations, the DMol3 program was used.[28] For the spin-density polarization calculation, DFT+U was adopted with a U of 3.3 eV.[29, 30]

Instruments and Characterization: The morphology was characterized by transmission electron microscopy (TEM, JEM1400) and high-resolution transmission electron microscopy (HRTEM, JEM2100). Powder X-ray diffraction (XRD) characterization of all samples was carried out on a Rigaku D/MAX 2550 diffractometer (Cu K radiation, λ=1.5406 Å) operating at 40 kV and 40 mA; data were collected in the range of 10-80° (2 theta). The scanning electron microscopy (SEM) analysis was performed using a TESCAN Nova III scanning electron microscope. The Brunauer-Emmett-Teller

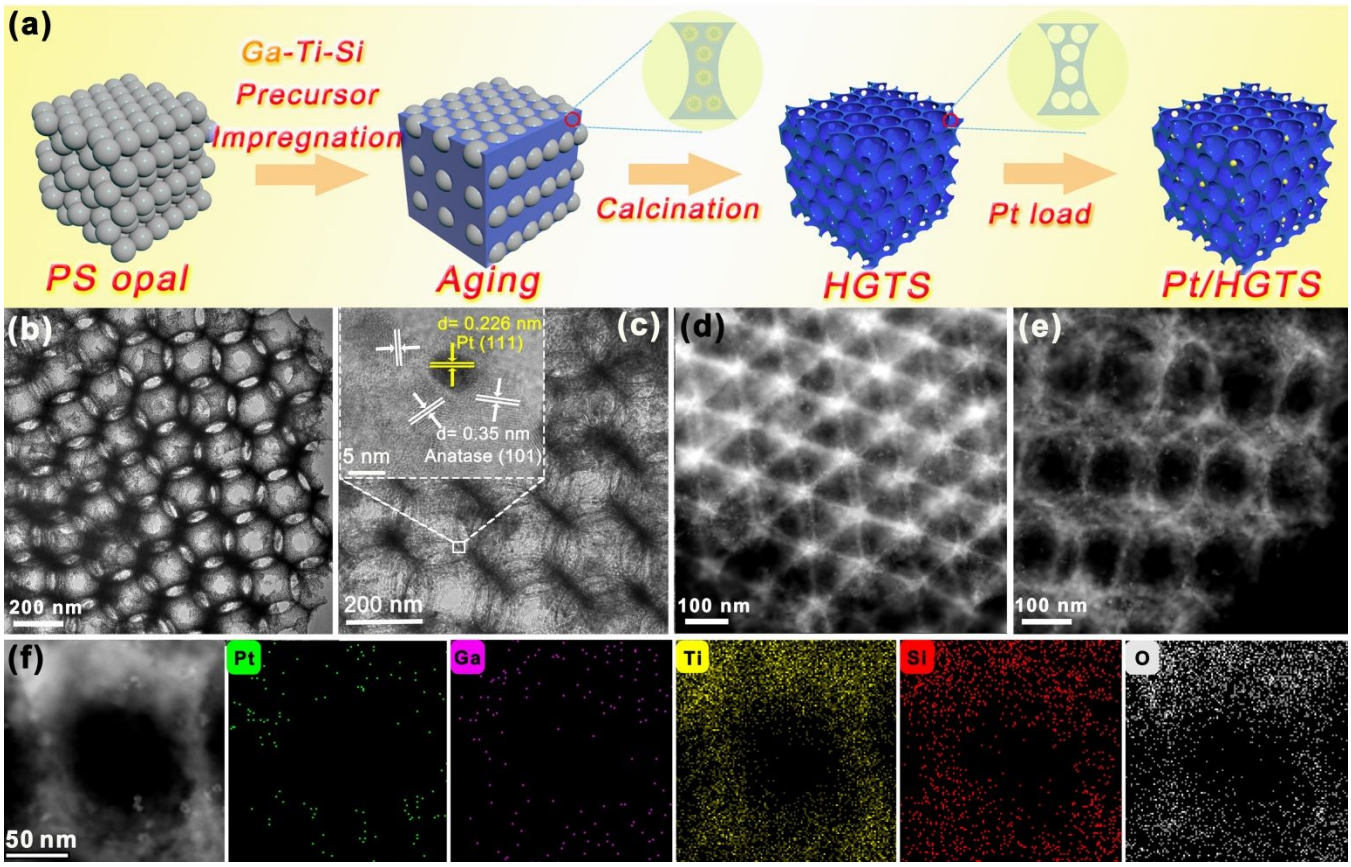

Figure 1. (a) Schematic illustration of the synthesis process for Pt/HGTS. (b) and (c) TEM images of Pt/HGTS (2%). (d) and (e) HAADF-STEM images of Pt/HGTS (2%). (f) HAADF-STEM image of Pt/HGTS (2%) and the corresponding elemental maps for Pt, Ga, Ti, Si, and O (scale bar: 50 nm). The theoretical Pt loading is 1 wt%, and the inset of Figure 1c is the corresponding HRTEM image of Pt/HGTS (2%).

(BET) surface area measurement was carried out by N_2 adsorption at 77 K using an ASAP2020 instrument. X-ray photoelectron spectroscopy (XPS) was performed on a Perkin-Elmer PHI 5000C ESCA system with Al Kα radiation operated at 250 W. The shift in the binding energy owing to the relative surface charging was corrected using the C 1s level at 284.4 eV as an internal standard. Electro-spin resonance spectrometry (ESR) was performed on a 100G-18KG/EMX-8/2.7 instrument. The UV-vis absorbance spectra of the dry-pressed disk samples were acquired using a Scan UV-vis spectrophotometer (Varian, Cary 500) equipped with an integrating sphere assembly, using $BaSO_4$ as the reflectance sample. The photoluminescence (PL) emission spectra of the solid catalysts were obtained using luminescence spectrometry (Cary Eclipse) at room temperature at an excitation wavelength of 350 nm. The electrochemical measurement was performed on an electrochemical analyzer (Zahner, Zennium) at room temperature. The standard three-electrode system was composed of a working electrode, a Pt wire counter electrode and a saturated calomel reference electrode. The working electrode was prepared by depositing a sample film on a F-doped SnO_2-Coated (FTO) glass. A 5-mg sample was dissolved in 0.5 mL of ethanol, and then 20 μL of solution was dropped on the FTO glass within an area of 1 cm^2 and dried at room temperature. The transient photocurrent response of the different samples was determined in a 0.5 M Na_2SO_4 aqueous solution under irradiation of a 300-W Xe lamp without the filter. The Mott-Schottky measurement was conducted in the potential range from -1.0 to 0.5 V (vs RHE) at a frequency of 1.0 kHz under the 300-W Xe lamp irradiation. The contents of Pt and Ga on the catalysts were analyzed by inductively coupled plasma atomic emission spectrometry (ICP-AES, Varian 710-ES, Agilent). Raman spectra were recorded on a Renishaw in Via-Reflex Raman microprobe system equipped with Peltier charge-coupled device detectors and a Leica microscope. A 532-nm laser was used as the excitation light source. High-angle annular dark-field scanning transmission electron microscopy (HAADF-STEM) imaging and elemental mapping were carried out on a JEM-2100F electron microscope operated at 200 kV.

RESULTS AND DISCUSSION

Figure 1a illustrates the synthesis process for Pt/HGTS. First, monodisperse polystyrene (PS) spheres with an average diameter of 355 nm (Figure S1) are used to form PS opals. Then, a Ga-Ti-Si precursor, with a fixed Ti/Si molar ratio of 4 and containing mesoporous template P123, is impregnated into the void of the PS opals (Scheme 1). The Ga-modified sample is marked as HGTS (x%), where x% represents the theoretical molar ratio of Ga/Ti. During the solvent evaporation and the subsequent aging process, the mesopores templated from P123 micelles are formed in the voids between the PS opals. PS and P123 are removed through calcination, forming the hierarchical macro-mesoporous HGTS. Pt nanoparticles are then loaded via a

photodeposition method using $H_2PtCl_6 \cdot 6H_2O$ as the precursor.

The transmission electron microscopy (TEM) image of Pt/HGTS (2%) (Figure 1b) clearly displays a typical inverse opal structure, demonstrating the successful replication of the PS opals. The hexagonally arranged macropores are well interconnected and have an average diameter of approx. 260 nm, which is favorable for the diffusion and transportation of molecules. The enlarged image shows that Pt nanoparticles (NPs) with a uniform size of approx. 4.4 nm are well dispersed on the framework surface (Figure 1c and Figure S2). The HRTEM image (Inset, Figure 1c) shows the lattice fringes of 0.27 nm and 0.35 nm, indexing to the (111) planes of Pt and the (101) planes of anatase.[31] High-angle annular dark-field scanning transmission electron microscopy (HAADF-STEM) verifies the uniform distribution of Pt particles (Figure 1d-e). The elemental maps of the macroporous framework reveal the homogeneous distribution of Pt, Ti, O, Si and Ga (Figure 1f and Figure S3). Moreover, all of the Pt/HGTS samples with various Ga/Ti ratios (1-5%) possess an ordered hierarchical porous arrangement and similar Pt sizes (Figure S4), indicating that Ga doping does not cause the deterioration of the porous structure or variation in the Pt size.

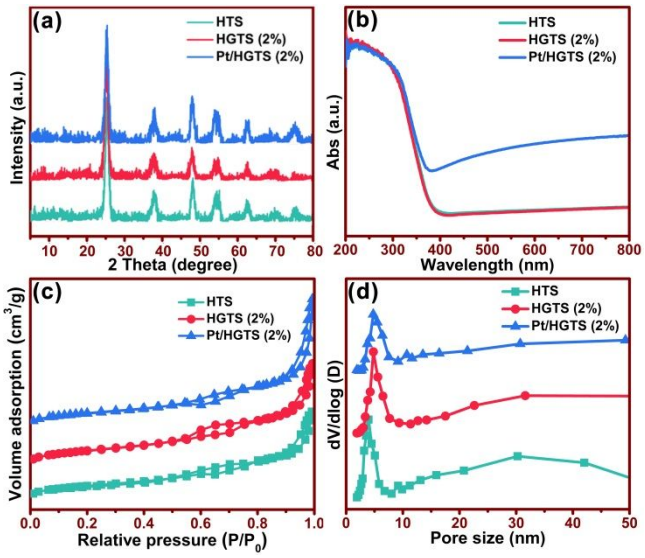

Figure 2. (a) XRD patterns, (b) UV-Vis DRS spectra, (c) nitrogen adsorption-desorption isotherms and (d) pore size distributions of HTS, HGTS (2%) and Pt/HGTS (2%).

The XRD patterns for HTS, HGTS (2%) and Pt/HGTS (2%) all have diffraction peaks at 25.3, 37.8, 48.0, 55.1, 62.7 and 75.0° (Figure 2a), which can be indexed to the (101), (004), (200), (211), (204) and (215) crystal facets of anatase phase (JCPDS No. 21-2172), respectively. Compared with the pattern for HTS, HGTS (2%) shows no other diffraction peaks, suggesting that Ga is possibly doped into the framework of HTS or forms a highly dispersed oxide species on the pore surface. Other Ga-modified samples show the same diffraction peaks (Figure S5). Compared with the pattern for pure HTS, the enlarged image indicates that the highest (101) diffraction peak shifts toward small angles with increasing Ga amount (Figure S6); this result suggests the substitution of Ga^{3+} for Ti^{4+} causes a lattice expansion since Ga^{3+} (0.076 nm) is larger than Ti^{4+} (0.068 nm).[32] Compared with the pattern for HTS, Pt/HGTS (2%) and other Pt-loaded samples do not show any diffraction peak for Pt, possibly due to the small particle size and good dispersion (Figure S7). The average TiO_2 crystallite size in HGTS (2%) is approx. 8.6 nm, as calculated from the Scherrer equation. The small crystallite size is attributed to the restricted growth of TiO_2 embedded in the mesoporous framework. The Raman spectra (Figure S8) show five representative peaks of anatase, where the peaks at 144, 196 and 636 cm^{-1} are attributed to the E_g mode and where the peaks at 396 cm^{-1} and 517 cm^{-1} are assigned to the B_{1g} mode and doublet of A_{1g}/B_{1g}.[33, 34] No peak attributed to Ga oxide species is found, further confirming that Ga is successfully doped into HTS.[35] The UV-Vis DRS spectra show that Ga doping has no effect on the bandgap of HTS (Figure 2b and Figure S9). The visible-light absorption intensity increases and the absorption edge of HTS slightly shifts to a longer wavelength after Pt loading (Figure 2b and Figure S10). Two capillary condensation steps can be seen in the N_2 adsorption-desorption isotherms (Figure 2c). The step at P/P_o=0.4-0.8 is attributed to mesopores, while the hysteresis loop at higher pressure (P/P_o=0.8-0.995) is from the macroporous cavities. The pore size distributions (Figure 2d) derived from the adsorption branch of the isotherms utilizing the BJH model show that the mesopore sizes are approximately 4.8 nm for HGTS (2%) and 4.9 nm for Pt/HGTS (2%). The specific surface areas of HGTS (2%) and Pt/HGTS (2%) are calculated to be 195 and 191 m^2g^{-1}, which indicate that Pt loading has no clear effect on the specific surface area and pore size distribution. Moreover, the tuning of the Ga percentage in the range of 1-5% does not cause evident variations in the absorption bands (Figures S9-S10) and porous characteristics of HGTS and Pt/HGTS (Figures S11-S12). The actual Pt loading percentage is approx. 0.25% for all Pt/HGTS (x%) samples, and the real Ga amount is approx. 50% of the theoretical Ga/Ti ratio (Table S1).

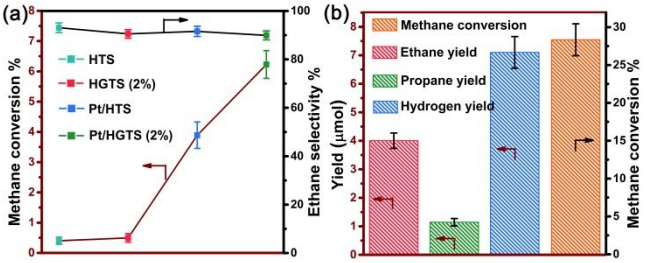

Figure 3. (a) Methane conversion and the corresponding selectivity towards ethane obtained in the photodriven NOCM reaction over various samples and under direct irradiation from a 300-W Xe lamp for 4 h. Samples from left to right: HTS, HGTS (2%), Pt/HTS, and Pt/HGTS (2%). (b) The ethane, propane, and hydrogen yields and the corresponding methane conversion from the photodriven NOCM reaction over Pt/HGTS (2%) under direct irradiation from a 300-W Xe lamp for 32 h. The error bars arise from values extracted from several measurements on multiple catalysts.

The photocatalytic NOCM performance of Pt/HGTS was tested at room temperature upon irradiation with a 300-W Xe lamp. No hydrocarbon product can be detected without photoirradiation or methane. Thermal desorption was used to ensure complete molecular desorption after the reaction, and its influence on the NOCM efficiency was excluded through a series of control experiments (Figure S13). All

Pt/HGTS samples are active for NOCM (Table S2). The highest CH_4 conversion percentage of approx. 6.24% is achieved within 4 h of irradiation of sample Pt/HGTS (2%) with 90.1% selectivity to ethane, corresponding to a conversion rate of 3.48 $\mu molg^{-1}h^{-1}$ (Figure 3a). The catalyst shows a high efficiency among those of reported catalysts (Table S3). An apparent quantum yield (AQY) of approx. 10^{-4} % is achieved on Pt/HGTS (2%) (Table S4). Decreasing or increasing the Ga content leads to a decrease in NOCM activity, while a higher Ga content deteriorates the selectivity to C_2H_6 (Table S2). Pt/HTS without Ga was prepared to understand the origin of the activity, and it shows a lower conversion efficiency of 3.92% (Figure 3a). The activity further decreases to 1.06% on Pt/P25, using commercial P25 as the carrier (Table S2). Moreover, P25 and the titanosilicate TS-1 are inactive for NOCM, while HTS, with the hierarchical pore structure, shows a low conversion rate of 0.41% (Figure 3a). To further understand the effect of hierarchical pores, a mesoporous GTS loaded with the same amount of Pt was synthesized, and it shows a lower activity than that of its hierarchical porous counterpart (Table S2), verifying the contribution from the interconnected hierarchical porous structure. The above results suggest that the loading of Pt is key to the NOCM activity, and the ordered hierarchical porous microarray, together with Ga doping, helps to improve the conversion efficiency. Furthermore, the stability of Pt/HGTS and the changes in product distribution were investigated by prolonging the irradiation time, using Pt/HGTS (2%) for the demonstration. The conversion percentage improves with the irradiation time and reaches approx. 28% after continuous irradiation for 32 h. The selectivity towards C_2H_6 decreases to 63.3% due to the formation of propane and a tiny amount of butane. Besides the hydrogen atoms in the hydrocarbon products, almost all of the remaining hydrogen atoms from CH_4 are released in the form of H_2, with a production rate of 36 $\mu molg^{-1}$. The hierarchical morphology and crystal structure of Pt/HGTS remain intact, as verified by the HRTEM image (Figure S14), demonstrating the excellent structural stability of the catalyst. We also carried out a recycling test of Pt/HGTS (2%) by venting and re-injecting the reactants after 4 h of irradiation. With repeated experiments, the conversion of methane and selectivity towards ethane decrease gradually (Figure S15), and after 4 reaction cycles, they are reduced to 52.4% and 81.7% of the original values obtained by the first NOCM reaction, respectively. Overall, the photocatalytic stability remains sound compared with that of previous reports.[22, 24] We assume that Pt accepts the photoinduced electrons from the semiconductor TiO_2 under light irradiation and is responsible for the initial CH_4 activation. However, the accumulated holes in TiO_2 may alter the Pt characteristics and gradually lead to the decreased conversion efficiency for methane and selectivity towards ethane.

To uncover the mechanism of Ga doping in enhancing NOCM activity, XPS spectroscopy was applied to study the surface atomic information. The refined Ti 2p XPS spectra of HGTS (x%) (Figure S16) reveal bimodal peaks at approximately 458.8 and 464.5 eV, which correspond to Ti $2p_{1/2}$ and Ti $2p_{3/2}$, respectively.[36] The Ga $2p_{2/3}$ spectrum is mainly characterized by a peak at 1118.3 eV (Figure S17), proving that the majority of surface gallium is in the Ga^{3+} state.[37] Figure 4a-d shows three O 1s peaks at 532.6, 531.5 and 530.1 eV, which are assigned to oxygen atoms from -OH bonds, neighboring to Vo and from the perfect lattice. The peak related to Vo shows negligible improvement upon Ga doping (Figure 4b), implying that the introduction of Ga does not readily alter the Vo concentration. This signal disappears after Pt loading

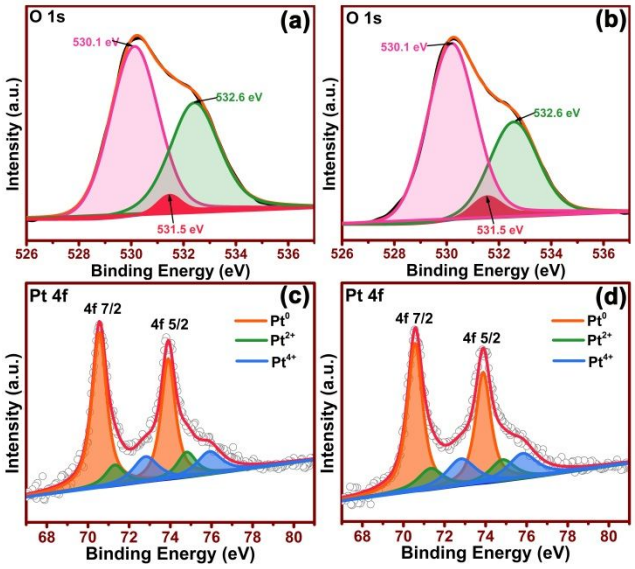

Figure 4. High-resolution XPS spectra of O 1s for (a) HTS and (b) HGTS and of Pt 4f for (c) Pt/HTS and (d) Pt/HGTS (2%).

(Figure S18), suggesting that Pt prefers to occupy Vo sites. Moreover, the Pt 4f spectrum (Figure 4c) indicates that both metallic and cationic Pt species are present on the surface of HTS; however, most Pt species on the catalyst surface are present in the metallic state. Furthermore, the presence of Ga results in a higher amount of cationic Pt (Table S5).

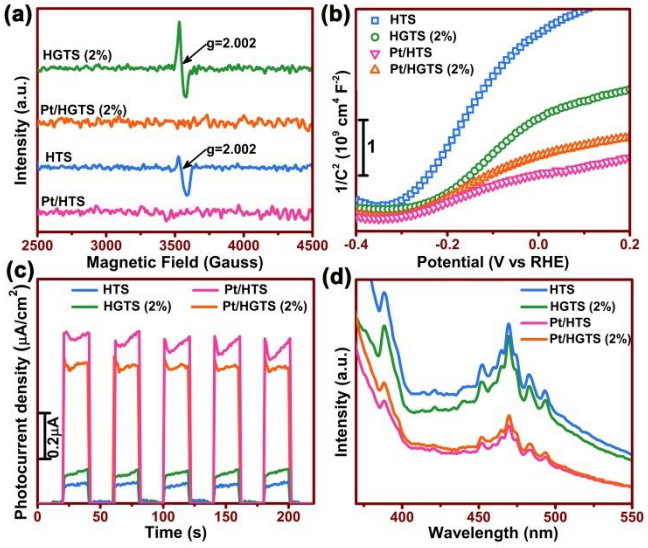

Figure 5. (a) EPR results for different samples. (b) Mott-Schottky plots for samples at frequencies of 1.0 kHz. (c) Transient photocurrent responses of different samples (300-W Xe lamp is used as the light source, and 0.5 M Na_2SO_4 is used as the electrolyte). (d) Room-temperature photoluminescence (PL) emission spectra of different samples (excitation wavelength is 350 nm).

EPR (electron paramagnetic resonance) was further employed to explore the influence of Ga doping on the electronic structure of Vo in TiO_2. The intense signal at g=2.002 for sample HGTS (2%) originates from the unpaired electron trapped by Vo (Figure 5a). Since the concentration of surface Vo does not show an apparent variation with Ga doping,

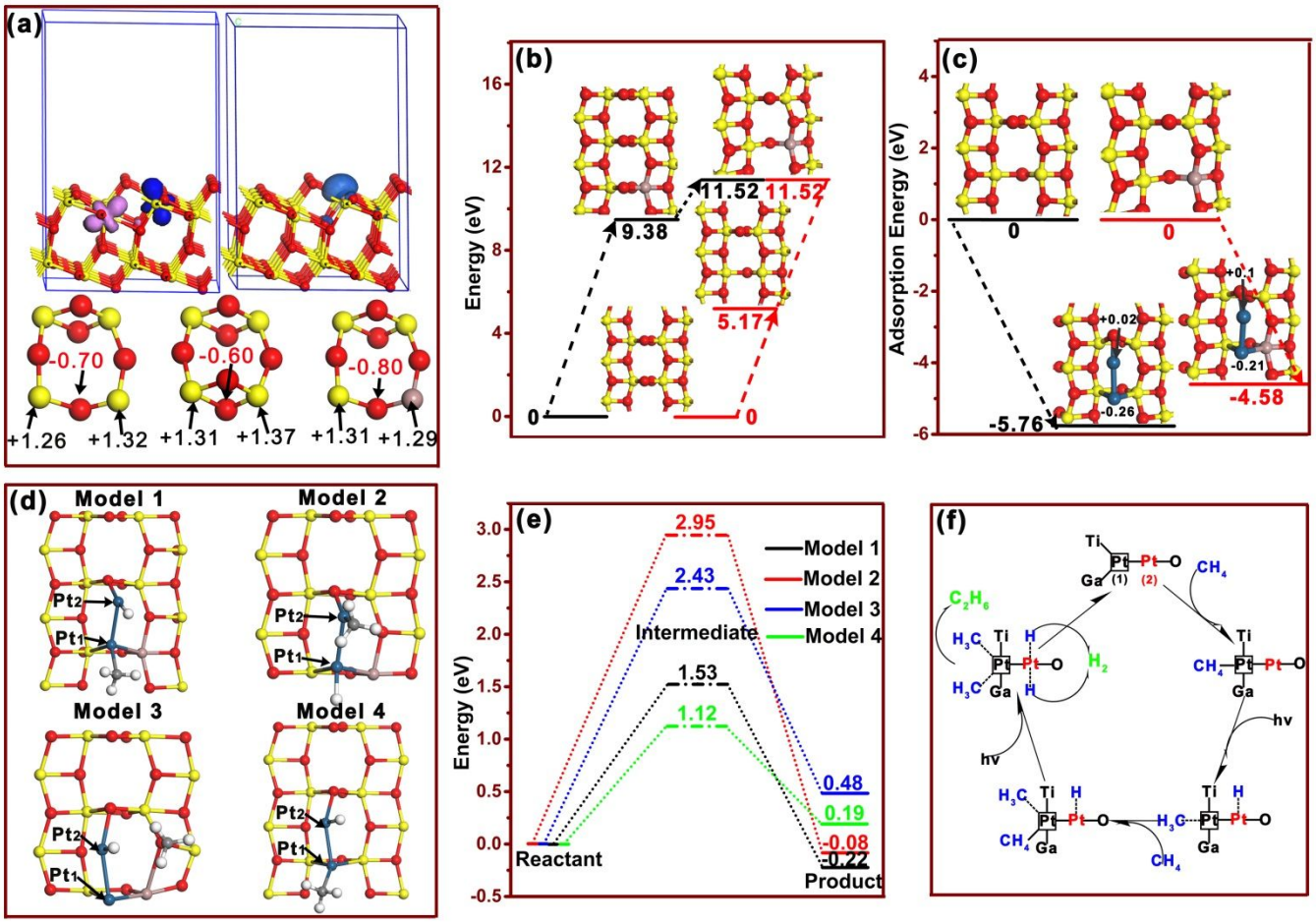

Figure 6. (a) Structures and polaron analysis of the anatase TiO_2 (101) surface with Vo (top left) and the anatase TiO_2 (101) surface with Vo and Ga substitution (top right). The structures and corresponding Mulliken charge analyses of surface atoms on different structures, from bottom left to bottom right, are: the anatase TiO_2 (101) surface with Vo, anatase TiO_2 (101) surface, and anatase TiO_2 (101) surface with Vo and Ga substitution. (b) Energies of the two routes for Ga substitutions of Ti_{5c} and Vo formation, black route: Ga substitutes for Ti_{5c} first and then forms Vo in TiO_2; red route: Ga substitutes for the Ti_{5c} neighboring the original Vo. (c) Adsorption energies for a Pt dimer adsorbed on defective TiO_2 with (red line) and without (black line) Ga substitution. (d) Optimized geometries of four models for C-H cleavage: (model 1) $-CH_3$ and -H are adsorbed on Pt_1 and Pt_2, (model 2) -H and $-CH_3$ are adsorbed on Pt_1 and Pt_2, (model 3) -H and $-CH_3$ are adsorbed on Pt_2 and the O neighboring Ga, and (model 4) the same as model 1 except there is no Ga substitution. (e) Reaction energy profiles of four models, where the black line refers to model 1, red line refers to model 2, blue line refers to model 3, and green line refers to model 4. Ti, O, Pt, Ga, C and H atoms are shown in yellow, red, royal, pink, gray and white colors, respectively. (f) The proposed molecular mechanism of the photocatalytic NOCM reaction.

according to the XPS spectra, it is highly possible that Ga doping alters the chemical state of the original Vo. As is known, the excess electrons formed from Vo in anatase TiO_2 tend to be localized on neighboring Ti. The above results suggest that the presence of Ga may be in favor of stabilizing the single-electron trapped Vo. The signal at g = 2.002 disappears after Pt loading, indicating the transfer of the excess electrons from Vo to Pt. This result is consistent with the XPS analysis that Pt nanoparticles prefer to grow on Vo sites.[38]

Photoelectrochemical and room-temperature photoluminescence (PL) analyses were further carried out to uncover the carrier characteristics. According to the Mott-Schottky plots (Figure 5b), all of the catalysts show positive slopes, indicating the n-type character of their electronic band structures. The electron carrier concentrations of HTS and HGTS (2%) are approx. 5.05×10^{20} cm^{-3} and 9.40×10^{20} cm^{-3} (Table S6), respectively, which indicate that Ga doping is beneficial for increasing the concentration of free excess electrons. Generally, Ga^{3+}, as a p-type dopant in the perfect TiO_2 lattice, is expected to form excess holes and decrease the concentration of excess electrons in TiO_2. Therefore, for the sample HGTS, Ga may prefer to substitute the Ti neighboring Vo over that in the perfect lattice, which

obstructs the electron transfer from Vo to neighboring Ti. The electron left at Vo may be more delocalized than that pinned at Ti and is responsible for the improved total density of free electron carriers. The deposition of metallic Pt causes a more significant increase in the free electron concentration, as observed in Pt/HTS (1.59×10^{21} cm^{-3}); however, this value is reduced to 1.54×10^{21} cm^{-3} on Pt/HGTS (2%). Further increasing the Ga percentage leads to a continuous decrease in the carrier concentration, while a lower Ga content (Pt/HGTS (1%)) results in a higher concentration of 1.67×10^{21} cm^{-3} (Figure S19). Similarly, the transient photocurrent response indicates that the loading of Pt on HTS causes a considerable signal improvement, which decreases on Pt/HGTS (2%) (Figure 5c). The response to the Ga doping content is similar to the result from the Mott-Schottky analysis, where 1% Ga doping improves the current intensity of Pt/HGTS but additional Ga doping leads to an intensity decrease (Figure S20). The PL spectra of the above samples also show the same tendency (Figure 5d and Figure S21). The peak located at 388 nm is attributed to the band-gap transition, the peaks at approximately 451 nm and 470 nm are from the band-edge free excitons, and the other two peaks at approximately 483 nm and 493 nm are related to bound excitons.[39, 40] The improved photoelectrochemical performance obtained after Pt loading, as demonstrated above, is attributed to the formation of a Mott-Schottky junction between Pt and TiO_2,[41] which can significantly accelerate the carrier separation. The electron-enriched Pt accounts for the enhanced NOCM activity of Pt/HTS. However, it should be noted that although Pt/HGTS (1%) with the lowest Ga doping presents the best carrier separation performance, the highest NOCM efficiency is achieved on Pt/HGTS (2%). The inconsistency between the photoelectric and NOCM efficiencies indicates that the photocatalytic NOCM is not simply determined by the separation efficiency of photoinduced charge carriers.

The DFT calculation was carried out to more deeply understand the effect of Ga doping on the chemical states of Vo and the adsorbed Pt (Figure 6). For the model, (1 0 1) facet-exposed TiO_2 slabs with and without a surface Vo formed from the 2-coordinated O (O_{2c}) are adopted. The slab with a Ti_{5c} next to Vo substituted by Ga is used to represent sample HGTS. The DFT+U calculation indicates that a polaron is formed at the surface Vo, where excess electrons are pinned at the neighboring Ti_{6c} and Ti_{5c} and accompanied by the lattice distortion (Figure 6a).[42] In contrast, the electron transfer from Vo to Ti_{6c} is blocked in the presence of Ga. Only one polaron is observed at the Ga site, with a more delocalized electron cloud (Figure 6a). The Mulliken charge analysis further verifies that the excess electrons from Vo tend to be localized at Ti_{5c} and Ti_{6c} on the (1 0 1) surface, decreasing the charge of Ti_{5c} and Ti_{6c} (Figure 6a). The electron transferred from Vo is reduced after the substitution of Ga for Ti_{5c}. Moreover, the energy required for Ga to substitute Ti_{5c} decreased approx. 3 eV in the presence of Vo, suggesting that Vo indeed favors the doping by Ga (Figure 6b). The above results are accordant with the results from XPS and EPR, further confirming that Ga doping next to Vo results in Vo with a trapped electron. Furthermore, the Pt dimer is used to explore both metal-metal and metal-support interactions, where Pt_1 occupies the Vo site and Pt_2 is adsorbed near a bridging O_{2c} site away from Vo.[43, 44] The adsorption energy of a Pt dimer at the surface Vo next to Ga is 1.18 eV positive to that without Ga (Figure 6c), but both are thermodynamically favorable. The neutral Pt_2 and electron-enriched Pt_1 are formed on TiO_2. In contrast, both Pt_1 and Pt_2 become more positively charged in the Ga-doped anatase TiO_2(1 0 1) slab, resulting in cationic Pt_2 and electron-enriched metallic Pt_1; this determination agrees well with the XPS result that Ga doping helps to form cationic Pt. We assume that Ga doping reduces the electron transfer from Vo to the adsorbed Pt. Therefore, the decrease in photoelectrochemical efficiency with increasing Ga should be related to the formation of a higher amount of cationic Pt.

Further DFT calculations were performed to understand the effect of Ga doping and the Pt state on the NOCM conversion. Four models for C-H cleavage were calculated (Figure 6d). First, the dissociated -CH_3 and -H are adsorbed on Pt_1 and Pt_2. Second, the dissociated -H and -CH_3 are adsorbed on Pt_1 and Pt_2. Third, -H and -CH_3 are adsorbed on Pt_2 and the O neighboring Ga. Fourth, the model is the same as model 1 except there is no Ga substitution (Pt/HTS). The C-H dissociation on Pt_1 and Pt_2 (models 1 or 2) is more thermodynamically favorable than on Pt_2 and O (model 3) according to the reaction energy (Figure 6e). Furthermore, model 1 with –H on cationic Pt_2 and –CH_3 on metallic Pt_1 is more kinetically favorable than models 2 and 3 according to the reaction barrier. We infer that the electron-deficient Pt_2 and electron-enriched Pt_1 result in a cationic-anionic active pair, which is more efficient for the dissociation of C-H bonds. Specifically, CH_4 can be more easily activated by metallic Pt_1, and the cationic Pt helps to abstract H. Additionally, compared with model 4, model 1 decreases the C-H dissociation energy by approx. 0.41 eV but slightly increases the reaction barrier. The decreased reaction barrier on Pt/HTS should be ascribed to the more negatively charged Pt_1 on TiO_2. However, considering the low reaction barriers on both Pt/HTS and Pt/HGTS, the reaction should be thermodynamically controlled, and Ga substitution helps to retard the reverse reaction. Furthermore, an excessive addition of Ga is found to not only reduce the photocatalytic conversion efficiency but also lead to the formation of more C_{2+} species (Table S2). This result verifies our assumption about the effect of Ga doping on the formation of cationic Pt that facilitates C-H cleavage but retards the photoinduced carrier separation. Based on the above results, the effect of Ga doping is summarized as follows: Ga tends to substitute Ti_{5c} neighboring Vo sites, which alters the electronic characteristics of Vo by blocking the electron transfer, leading to the formation of Vo with an unpaired electron. Furthermore, Ga doping reduces the electron transfer from Vo to the adsorbed Pt, resulting in the formation of a higher amount of cationic Pt. The cationic-metallic Pt pairs provide active sites for C-H dissociation. However, when a higher amount of cationic Pt is formed from the increasing Ga doping, the NOCM efficiency is decreased due to the reduced carrier separation efficiency. Therefore, an appropriate amount of Ga doping next to Vo is required to achieve the cooperation between charge separation and C-H activation. Modulation of the Vo concentration is expected to further enhance the cooperation effect. Based on the results and discussion above, we propose a mechanism for the photocatalytic NOCM reaction on Pt/HGTS (Figure 6f). First, CH_4 is activated by the electron-enriched metallic Pt, and then the C-H bond is dissociated under light irradiation. The

resultant -CH_3 and -H are adsorbed on Pt_1 and Pt_2, respectively. Second, another CH_4 is activated and dissociated in the same way as the first CH_4 (Figure S22). Then, the two -H intermediates generate a H_2 molecule, and the two -CH_3 intermediates generate a C_2H_6 molecule. Finally, the formed C_2H_6 and H_2 are desorbed to complete a cycle reaction.

CONCLUSION

In summary, Pt-loaded and Ga-doped macro-mesoporous TiO_2-SiO_2 composites were fabricated and applied to the photodriven NOCM reaction. Ga doping leads to the formation of a higher amount of cationic Pt but decreases the carrier separation efficiency. Through the appropriate tuning of the Ga doping amount, a high methane conversion rate of 3.48 $\mu molg^{-1}h^{-1}$ can be achieved due to the promoted C-H cleavage by cationic Pt and the effective separation of photo-induced charge carriers by metallic Pt. It is expected that this work will offer significant guidance to the future design of efficient photocatalysts toward methane conversion, as achieved through modulation of the surface atomic arrangement and electronic characteristics of semiconductor composites.

ASSOCIATED CONTENT

Supporting Information. HAADF-STEM, TEM and SEM images, XRD patterns, Raman spectra, UV-Vis DRS spectra, BET result, HRTEM image, transient photocurrent responses, room-temperature photoluminescence (PL) emission spectra, XPS results, and a comparison of the photodriven methane conversions of different samples.

AUTHOR INFORMATION

Corresponding Author

* wlz@ecust.edu.cn
* jlzhang@ecust.edu.cn

ACKNOWLEDGMENT

This work was supported by the National Natural Science Foundation of China (21673073, 21677048 and 5171101651), the Science and Technology Commission of Shanghai Municipality (18520710200, 16JC1401400, 17520711500), Shanghai Pujiang Program (18PJD012), the PetroChina Innovation Foundation (2015D-5006-0402) and the Fundamental Research Funds for the Central Universities (222201717003, 22221818014).

REFERENCES

(1) Schwach, P.; Pan, X.; Bao, X. Direct Conversion of Methane to Value-Added Chemicals over Heterogeneous Catalysts: Challenges and Prospects. Chem. Rev. **2017**, *117*, 8497-8520.

(2) Yoshida, H.; Hirao, K.; Nishimoto, J.; Shimura, K.; Kato, S.; Itoh, H.; Hattori, T. Hydrogen Production from Methane and Water on Platinum Loaded Titanium Oxide Photocatalysts. J. Phys. Chem. C **2008**, *112*, 5542-5551.

(3) Yoshida, H.; Kato, S.; Hirao, K.; Jun-Ichi, N.; Hattori, T. Photocatalytic Steam Reforming of Methane over Platinum-loaded Semiconductors for Hydrogen Production. Chem. Lett. **2007**, *36*, 430-431.

(4) Shimura, K.; Kato, S.; Yoshida, T.; Itoh, H.; Hattori, T.; Yoshida, H. Photocatalytic Steam Reforming of Methane over Sodium Tantalate. J. Phys. Chem. C **2010**, *114*, 3493-3503.

(5) Shimura, K.; Kawai, H.; Yoshida, T.; Yoshida, H. Bifunctional Rhodium Cocatalysts for Photocatalytic Steam Reforming of Methane over Alkaline Titanate. ACS Catal. **2012**, *2*, 2126-2134.

(6) Chanmanee, W.; Islam, M. F.; Dennis, B. H.; Macdonnell, F. M. Solar Photothermochemical Alkane Reverse Combustion. P. Natl. Acad. Sci. USA. **2016**, *113*, 2579-2584.

(7) Guo, X.; Fang, G.; Li, G.; Ma, H.; Fan, H.; Yu, L.; Ma, C.; Wu, X.; Deng, D.; Wei, M.; Tan, D.; Si, R.; Zhang, S.; Li, J.; Sun, L.; Tang, Z.; Pan, X.; Bao, X. Direct, Nonoxidative Conversion of Methane to Ethylene, Aromatics, and Hydrogen. Science **2014**, *344*, 616-619.

(8) Yoshida, H.; Matsushita, N.; Kato, Y.; Hattori, T. Active Sites in Sol-gel Prepared Silica-alumina for Photoinduced Non-oxidative Methane Coupling. Phys. Chem. Chem. Phys. **2002**, *4*, 2459-2465.

(9) Yuliati, L.; Hamajima, T.; Hattori, T.; Yoshida, H. Nonoxidative Coupling of Methane over Supported Ceria Photocatalysts. J. Phys. Chem. C **2008**, *112*, 7223-7232.

(10) Choudhary, V. R.; Kinage, A. K.; Choudhary, T. V. Low-Temperature Nonoxidative Activation of Methane over H-Galloaluminosilicate (MFI) Zeolite. Science **1997**, *275*, 1286-1288.

(11) Shimura, K.; Yoshida, H. Semiconductor Photocatalysts for Non-oxidative Coupling, Dry Reforming and Steam Reforming of Methane. Catal. Surv. Asia. **2014**, *18*, 24-33.

(12) Yuliati, L.; Itoh, H.; Yoshida, H. Photocatalytic Conversion of Methane and Carbon Dioxide over Gallium Oxide. Chem. Phys. Lett. **2008**, *452*, 178-182.

(13) Teramura, K.; Iguchi, S.; Mizuno, Y.; Shishido, T.; Tanaka, T. Photocatalytic Conversion of CO_2 in Water over Layered Double Hydroxides. Angew. Chem. Int. Ed. **2012**, *124*, 8132-8135.

(14) Dong, C.; Xing, M.; Zhang, J. Economic Hydrophobicity Triggering of CO_2 Photoreduction for Selective CH_4 Generation on Noble-Metal-Free TiO_2-SiO_2. J. Phys. Chem. Lett. **2016**, *7*, 2962-2966.

(15) Dong, C.; Xing, M.; Zhang, J. Double-cocatalysts Promote Charge Separation Efficiency in CO_2 Photoreduction: Spatial Location Matters. Mate. Horiz. **2016**, *3*, 608-612.

(16) Yoshida, H.; Matsushita, N.; Yuko Kato, A.; Hattori, T. Synergistic Active Sites on SiO_2-Al_2O_3-TiO_2 Photocatalysts for Direct Methane Coupling. J. Phys. Chem. B **2003**, *107*, 8355-8362.

(17) Kato, Y.; Matsushita, N.; Yoshida, H.; Hattori, T. Highly Active Silica-alumina-titania Catalyst for Photoinduced Non-oxidative Methane Coupling. Catal. Commun. **2002**, *3*, 99-103.

(18) Yuliati, L.; Hattori, T.; Yoshida, H. Highly Dispersed Magnesium Oxide Species on Silica as Photoactive Sites for Photoinduced Direct Methane Coupling and Photoluminescence. Phys. Chem. Chem. Phys. **2005**, *7*, 195-201.

(19) Yoshida, H.; Chaskar, M. G.; Kato, Y.; Hattori, T. Active Sites on Silica-supported Zirconium Oxide for Photoinduced Direct Methane Conversion and Photoluminescence. J. Photochem. Photobiol. A. **2003**, *160*, 47-53.

(20) Yuliati, L.; Hamajima, T.; Hattori, T.; Yoshida, H. Highly Dispersed Ce(III) Species on Silica and Alumina as New Photocatalysts for Non-oxidative Direct Methane Coupling. Chem. Commun. **2005**, *38*, 4824-4826.

(21) Kato, Y.; Yoshida, H.; Satsuma, A.; Hattori, T. Photoinduced Non-oxidative Coupling of Methane over H-zeolites Around Room Temperature. Micropor. Mesopor. Mat. **2002**, *51*, 223-231.

(22) Li, L.; Cai, Y. Y.; Li, G. D.; Mu, X. Y.; Wang, K. X.; Chen, J. S. Synergistic Effect on the Photoactivation of the Methane C-H Bond over Ga^{3+}-Modified ETS-10. Angew. Chem. Int. Ed. **2012**, *51*, 4702-4706.

(23) Chen, X.; Li, Y.; Pan, X.; Cortie, D.; Huang, X.; Yi, Z. Photocatalytic Oxidation of Methane over Silver Decorated Zinc Oxide Nanocatalysts. Nat. Commun. **2016**, *7*, 12273.

(24) Meng, L.; Chen, Z.; Ma, Z.; He, S.; Hou, Y.; Li, H.; Yuan, R.; Huang, X.; Wang, X.; Wang, X.; Long, J. Gold Plasmon-induced Photocatalytic Dehydrogenative Coupling of Methane to Ethane on Polar Oxide Surfaces. Energy Environ. Sci. **2018**, *11*, 294-298.

(25) Selcuk, S.; Selloni, A. Facet-dependent Trapping and Dynamics of Excess Electrons at Anatase TiO_2 Surfaces and Aqueous Interfaces. Nat. Mat. **2016**, *15*, 1107-1113.

(26) Clark, S. J.; Segall, M. D.; Pickard, C. J.; Hasnip, P. J.; Probert, M. J.; Refson, K.; Payne, M. C. First Principles Methods Using CASTEP. Z. Krist-Cryst. Mater. **2005**, *220*, 567-570.

(27) Perdew, J. P.; Burke, K.; Ernzerhof, M. Generalized Gradient Approximation Made Simple. Phys. Rev. Lett. **1996**, *77*, 3865.

(28) Delley, B. Phys An All-electron Numerical Method for Solving the Local Density Functional for Polyatomic Molecules. J. Chem. Phys. **1990**, *92*, 508-517.

(29) Delley, B. From Molecules to Solids with the DMol3 Approach. J. Chem. Phys. **2000**, *113*, 7756-7764.

(30) Dudarev, S. L.; Botton. G. A.; Savrasov. S. Y.; Humphreys, C. J.; Sutton, A. P. Electron-energy-loss Spectra and the Structural Stability of Nickel Oxide: An LSDA+U study. Phys. Rev. B **1998**, *57*, 1505-1509.

(31) Wei, Y.;Jiao, J.; Zhen, Z.; Zhong, W.; Li, J.; Liu, J.; Jiang, G. Duan, A.; 3D Ordered Macroporous TiO_2-supported Pt@CdS Core-shell Nanoparticle: Design, Synthesis and Efficient Photocatalytic Conversion of CO_2 with Water to Methane. J. Mater. Chem. A **2015**, *3*, 11074-11085.

(32) Yang, J.; Liu, R.; Huang, S.; Shao, Y.; Huang, Y.; Yu, Y. Enhanced Photocatalytic Activity and Stability of Interstitial Ga-doped CdS: Combination of Experiment and Calculation. Catal. Today **2014**, *224*, 104-113.

(33) Salari, M.; Konstantinov, K.; Liu, H. K. Enhancement of the Capacitance in TiO_2 Nanotubes through Controlled Introduction of Oxygen Vacancies. J. Mater. Chem. **2011**, *21*, 5128-5133.

(34) Sun, L.; Li, J.; Wang, C. L.; Li, S. F.; Chen, H. B.; Lin, C. J. An Electrochemical Strategy of Doping Fe^{3+} into TiO_2 Nanotube Array Films for Enhancement in Photocatalytic Activity. Sol. Energy Mater. Sol. Cells **2009**, *93*, 1875-1880.

(35) Wang, X.; Xu, Q.; Li, M.; Shen, S.; Wang, X.; Wang, Y.; Feng, Z.; Shi, J.; Han, H.; Li, C. Photocatalytic Overall Water Splitting Promoted by an α-β Phase Junction on Ga_2O_3. Angew. Chem. Int. Ed. **2012**, *124*, 13266-13269.

(36) Nie, L.; Yu, J.; Li, X.; Cheng, B.; Liu, G.; Jaroniec, M. Enhanced Performance of NaOH-modified Pt/TiO_2 toward Room Temperature Selective Oxidation of Formaldehyde. Environ. Sci. technol. **2013**, *47*, 2777-2783.

(37) Fang, Y.; Su, X.; Bai, X.; Wu, W.; Wang, G.; Xiao, L.; Yu, A. Aromatization over Nanosized Ga-containing ZSM-5 Zeolites Prepared by Different Methods: Effect of Acidity of Active Ga Species on the Catalytic Performance. J. Energ. Chem. **2017**, *26*, 768-775.

(38) Hirakawa, H.; Hashimoto, M.; Shiraishi, Y.; Hirai, T. Photocatalytic Conversion of Nitrogen to Ammonia with Water on Surface Oxygen Vacancies of Titanium Dioxide. J. Am. Chem. Soc. **2017**, *139*, 10929-10936.

(39) Yu, J.; Qi, L.; Jaroniec, M. Hydrogen Production by Photocatalytic Water Splitting over Pt/TiO_2 Nanosheets with Exposed (001) Facets. J. Phys. Chem. C **2010**, *114*, 13118-13125.

(40) Xiang, Q.; Lv, K.; Yu, J. Pivotal Role of Fluorine in Enhanced Photocatalytic Activity of Anatase TiO_2 Nanosheets with Dominant (0 0 1) Facets for the Photocatalytic Degradation of Acetone in Air. Appl. Catal., B **2010**, *96*, 557-564.

(41) Yu, X.; Shavel, A.; An, X.; Luo, Z.; Ibáñez, M.; Cabot, A. Cu_2ZnSnS_4-Pt and Cu_2ZnSnS_4-Au Heterostructured Nanoparticles for Photocatalytic Water Splitting and Pollutant Degradation. J. Am. Chem. Soc. **2014**, *136*, 9236-9239.

(42) Yang, Y.; Yin, L. C.; Gong, Y; Niu, P; Wang, J. Q.; Gu, L; Chen, X.; Liu, G.; Wang, L.; Cheng, H. M. An Unusual Strong Visible-Light Absorption Band in Red Anatase TiO_2 Photocatalyst Induced by Atomic Hydrogen-Occupied Oxygen Vacancies. Adv. Mater. **2018**, *30*, 1704479.

(43) Han, Y.; Liu, C. J.; Ge, Q. Interaction of Pt Clusters with the Anatase TiO_2(101) Surface: A First Principles Study. J. Phys. Chem. B **2006**, *110*, 7463-7472.

(44) Han, Y.; Liu, C. J.; Ge, Q. Effect of Surface Oxygen Vacancy on Pt Cluster Adsorption and Growth on the Defective Anatase TiO_2(101) Surface. J. Phys. Chem. C **2007**, *111*, 16397-16404.

For Table of Contents Only